Conceptual frame rationalizing the self-stabilization of H-USY zeolites in hot liquid water

Conceptual Frame Rationalizing the Self-Stabilization of Ru/H-USY Zeolites in Hot Liquid Water

Thijs Ennaert[†§], Jan Geboers[†§], Elena Gobechiya[†], Christophe M. Courtin[‡], Mert Kurttepeli[‖], Kristof Houthoofd, Christine E.A. Kirschhock[†], Gustaaf van Tendeloo[‖], Pieter C.M.M. Magusin[†], Sara Bals[‖], Pierre A. Jacobs[†] and Bert F. Sels[†,*]

[†] Centre for Surface Chemistry and Catalysis, KU Leuven, Kasteelpark Arenberg 23, 3001 Heverlee, Belgium

[‡] Laboratory of Food Chemistry and Biochemistry & Leuven Food Science and Nutrition Research Centre (LFoRCe), KU Leuven, Kasteelpark Arenberg 20, 3001 Heverlee, Belgium

[‖] Electron Microscopy for Materials Science (EMAT), Universiteit Antwerpen, Groenenborgerlaan 171, 2020 Antwerpen, Belgium

USY Zeolites, Faujasite, Stability, Self-Stabilization, Hot Liquid Water, Hydrothermal, ^{27}Al MQMAS NMR, Infrared Spectroscopy, Biomass, Cellulose, Sorbitol, Bifunctional Catalysis.

Supporting Information Placeholder

Abstract: The wide range of liquid-phase reactions required for the catalytic conversion of biomass compounds into new bio-platform molecules, defines a new set of challenges for the development of active, selective and stable catalysts. The potential of bifunctional Ru/H-USY catalysts for conversions in hot liquid water (HLW) is assessed in terms of physicochemical stability and long-term catalytic performance of acid sites and noble metal functionality as probed by hydrolytic hydrogenation of cellulose. It is shown that zeolite desilication is the main catalyst degradation mechanism in HLW. USY zeolite stability depends on two main parameters, *viz.* framework and extra-framework aluminum content, the former protecting the zeolite lattice by counteracting hydrolysis of framework bonds, the latter when located at the external crystal surface preventing solubilization of the zeolite framework, due to their low water-solubility. Hence, the hot liquid water stability of commercial H-USY zeolites, in contrast to their steam stability, increased with decreasing Si/Al ratio. As a result, mildly steamed USY zeolites containing a high amount of both Al species exhibit the highest resistance to HLW. During an initial period of transformations, Al-rich zeolites form protective extra-framework Al species at the outer surface, stabilizing the framework. A critical bulk Si/Al ratio of 3 was determined whereby USY zeolites with a lower Si/Al ratio will self-stabilize over time. Besides, due to the initial transformation period, the accessibility of the catalytic active sites is extensively enhanced resulting in a material that is more stable and drastically more accessible to large substrates than the original zeolite. When these findings are applied in the hydrolytic hydrogenation of cellulose, unprecedented nearly quantitative hexitol yields were obtained with a stable catalytic system.

INTRODUCTION

In contemporary catalyst research, much effort is being devoted to the conversion of biomass into value-added chemicals and fuels.[1] In an extension of their success in refinery and petrochemical processes, zeolite catalysts have shown excellent performance in a wide range of biomass-related reactions. Multiple examples have been reported like hydrolytic hydrogenation of starch and cellulose, lignin and biofuel upgrading, conjugation of fats and oils and deoxygenation of bio-derived molecules like glycerol and fatty acids.[2] Although the success of zeolites as catalysts is often based on the strong acidity of the protonated form, they also have shown to be excellent carriers for metal catalysts, opening the way to bifunctional catalysis.[3] Moreover, owing to spatial constrictions in their micropores, zeolites can exhibit shape selectivity as well.[4]

Due to their importance as catalysts in industrial gas-phase processes and to their often required regeneration with steam, zeolite steam stability has been studied extensively. Silica-rich hydrogen zeolites prepared through 'steaming' and/or treatment with mineral acid, show the required steam stability.[5] In this process, the zeolite framework is dealuminated, Si-O-Al bonds are hydrolyzed, and tetrahedrally coordinated Al (**FAl**) is extracted from the zeolite framework and is deposited mostly as octahedrally coordinated mono- and even oligomeric Al-O extra-framework (**EFAl**) species. Al extraction can lead to local disintegration of the zeolite framework, forming large mesopores. Furthermore, mobile Si species may partly heal framework defects left by extracted Al,[6] yielding highly crystalline, mesoporous zeolites with an increased framework Si/Al ratio and improved accessibility of acid sites. Such materials are

often referred to as 'ultrastable' (**US**), *viz.* USY zeolite. Residual EFAL adds Lewis acidity and seems to further enhance stability of such zeolites.[5a] It can be selectively removed from the material by washing at room temperature with (diluted aqueous) mineral acid.[5d]

In contrast to crude oil fractions, biomass containing high molecular weight components like (hemi)cellulose or lignin, is highly oxygenated, reducing their vapor pressure. Therefore, numerous catalytic conversions in future biorefineries will take place in the liquid phase, often even in hot liquid water (**HLW**). Hence, zeolite stability in HLW is becoming an increasingly important issue.[7] Several studies appeared investigating the physicochemical transformation of zeolites in such conditions,[2k, 8] showing that, whereas zeolite stability in steam is well understood, this is not necessarily the case in HLW.

The HLW stability of a zeolite appears depending on topology and nature and amount of charge compensating cations. Dense topologies like MFI and MOR are stable in water up to at least 473 K, while more open structures like BEA and FAU are easily transformed into amorphous materials.[8d] Interestingly, these investigations reported that the correlation between Si/Al ratio and stability in HLW does not always parallel that found during steaming. In contrast to stability during steaming, that of zeolite Y in HLW was reported to decrease with increasing overall Si/Al ratio.[8b, 8d, 8e] In a few studies, however, zeolite Y's HLW stability has been claimed to increase with increasing Si/Al ratio.[2k, 8g, 9] These contrasting claims clearly point to the absence of a conceptual understanding of HLW stability in terms of zeolite physicochemical properties.

In the present study, the fate of the faujasite topology was followed in conditions allowing acid-catalyzed depolymerization of cellulose. A series of H-USY zeolites with varying Si/Al ratio was extensively characterized before and after treatment in HLW using ICP, (pyridine probed) FTIR, N_2 physisorption, 1D MAS NMR, 2D MAS NMR, XRD, HAADF STEM and STEM-EDX. In addition, stability of the most promising material was assessed over a longer time. A conceptual frame results rationalizing and predicting the stability of H-USY zeolites in HLW. Due to the importance of zeolites as metal carriers in catalysis, stability of zeolite-supported ruthenium particles in HLW is addressed as well.

Characterization data were then correlated with the performance of Ru-loaded H-USY as bifunctional catalysts. For a comprehensive analysis, a well-understood, bifunctionally catalyzed reaction, *viz.* the previously reported one-pot aqueous hydrolytic hydrogenation of cellulose by Ru/H-USY in an aqueous mmolar solution of HCl was selected.[2b] For this reason, zeolite stability in HLW doped with mmolar amounts of HCl was compared to that in pure HLW.

EXPERIMENTAL

Materials

Y and USY zeolites were purchased from Zeolyst Int. and Siral30, an amorphous silica-alumina with Al_2O_3:SiO_2 = 70:30, was received from Sasol. An overview of sample nomenclature and pretreatment of the USY zeolites used in this study is presented in Table 1 and in the Supporting Information (SI). For clarity, all zeolites are denoted with a sample code based on their framework T atom fraction (Table 1). The procedure for preparation of Ru/H-USY catalysts has been reported earlier[2b] (see also SI). Microcrystalline cellulose, Avicel PH-101, obtained from Sigma-Aldrich was ball milled in a Fritsch Pulverisette and characterized by XRD, FTIR, ^{13}C CP MAS NMR and SEM according to reported procedures.[10]

Treatment of H-USY in HLW

Samples of the zeolite carrier of the catalysts used in cellulose catalysis, were pretreated in the same way as the (Ru) catalysts. 0.5 g H-USY zeolite and 50 ml 0.96 mM aqueous HCl (ChemLab) solution were loaded in a 100 ml stainless steel autoclave (Parr Instruments Co.), flushed with N_2 and heated at 463 K under stirring at 750 rpm. Afterwards, it was pressurized with hydrogen up to 5 MPa. It should be stressed that treatment in HLW in the present study also could imply the simultaneous presence of mM amounts of HCl. As the nature of the charge-compensating cation may influence zeolite stability in HLW and the catalyst fate for acid catalysis is aimed, only protonated zeolites of the H-USY family have been used in this work (calcination conditions see SI). The treatment was continued for 24 h, thus mimicking exactly a cellulose hydrolysis experiment in absence of cellulose in the reaction medium and Ru on the catalyst.

Physicochemical characterization

After treatment in HLW, Si and Al concentration in solution was analyzed with an Ultima ICP-AES apparatus equipped with a Burgener atomizer and a radial optic detector (polychromator). Argon was used as plasma source and carrier gas. The set-up was also used to analyze Si and Al concentration of zeolite powders after destruction in $LiBO_2$ at 1,273 K, followed by dissolution in concentrated HNO_3.

X-Ray diffraction patterns were recorded at room temperature on a STOE STADI MP diffractometer with a linear position sensitive detector (PSD) (6 °2θ window) from 4 to 60 °2θ, with a step width of 0.5 °, internal PSD resolution of 0.01 °, and a counting time of 200 s per step. The measurements were performed in Debye-Sherrer mode at room temperature using $CuK\alpha_1$ radiation with λ = 1.54056 Å selected by means of a Ge(111) monochromator. WinXpow software (STOE & CIE GmbH 2009) was employed to calculate the crystallinity index, i.e. the crystallinity of each sample after treatment in HLW relative to that of the untreated parent sample in deammoniated form (information in SI).

Porosity of the samples after pretreatment in N_2 at 673 K for 10 h, were derived from a nitrogen adsorption-desorption isotherm at 77 K using a Micromeritics *TriStar 3000*. Usually, 30 nitrogen uptake points were needed before nitrogen saturation pressure was reached. Desorption occurred stepwise till saturation before proceeding to the next step. Whereas the micropore volume was calculated from the t-plot, the mesopore volume was taken as the difference between total pore

volume and micropore volume. The error on the total pore volume and micropore volume was 10 and 3 %, respectively.

Table 1. Overview of pretreatment and composition of H-USY zeolites.

Sample code	Zeolite	Steaming	Acid wash	Bulk Si/Al[a]	Si/FAl[b]	FAl/(Si+FAl) x 100[c]
Y25[d]	CBV300	/	/	2.6	3.0	25
USY19	CBV500	1 x (mild)	/	2.6	4.4	19
USY16	CBV600	1 x	/	2.8	5.2	16
USY9	CBV712	1 x	Mild	5.8	10.0	9
USY6	CBV720	2 x	Extensive	13.0	16.7	6
USY3	CBV760	2 x	Extensive	30.0	34.9	3

[a] data from supplier; [b] calculated based on ICP and ^{27}Al MAS NMR data (*vide infra*), according to the method described by Remy et al.[11], [c] share of framework Al in total T atom content. [d] NH_4-Y zeolite deammoniated under flowing nitrogen at 673 K.

The samples for transmission electron microscopy (TEM) characterization were prepared by crushing the powder in ethanol and depositing drops of the suspension on a copper grid covered with a holey carbon film. High-angle annular dark field scanning transmission electron microscopy (HAADF-STEM) images and energy dispersive X-ray (EDX) spectroscopy maps were collected using a FEI Titan microscope operated at 200 kV and equipped with a probe aberration corrector and a Super-X detector. Tilt series of 2D HAADF-STEM images were acquired with 2° tilt increments over an angular range of ± 74 ° using a Fischione 2020 single tilt holder. The 3D reconstruction of the zeolitic particles was carried out using the simultaneously iterative reconstruction technique.[12]

FTIR spectra with a resolution of 2 cm^{-1} were determined on a Nicolet 6700 spectrometer with a DTGS detector, requiring accumulation of 128 scans per spectrum. Self-supported zeolite wafers of about 10 mg/cm^2 positioned in a temperature-controlled vacuum cell with ZnSe windows, were dried at 673 K during 1 h. Afterwards, a FTIR spectrum was scanned at 423 K. Zeolite acid density was determined by FTIR-monitored adsorption of pyridine vapor. After pyridine (Acros Organics) adsorption at 323 K for 10 min, the sample was heated to 423 K and evacuated during an additional 20 min (calculation method given in SI).

All ^{27}Al magic angle spinning nuclear magnetic resonance (MAS NMR) experiments were performed with a Bruker DSX400 spectrometer (B_0 = 9.4 T) on fully hydrated samples, packed into 2.5 mm zirconia rotors spun at 20 - 25 kHz. The ^{27}Al resonance frequency is at 104.3 MHz. A 0.1 M aqueous solution of $Al(NO_3)_3.9H_2O$ was used for calibrating the chemical shift scale. 36,000 scans were accumulated with an interpulse time of 100 ms. To calculate the relative contribution of different Al species, spectra were deconvoluted using DMFit 2009.[13] For ^{27}Al multi quantum magic angle spinning (MQMAS) NMR, the triple-pulse sequence p_1-t_1-p_2-τ-p_3-t_2 was used with hard pulses p_1 of 1.5 μs and p_2 of 0.5 μs at a nutation frequency of 200 kHz, and third soft pulse of 20 μs (12.5 kHz). The z-filter delay τ was 40 μs, and the evolution-time t_1 increment was 40 μs. The sample rotation rate was 25 kHz. 64 traces of 240 scans each were accumulated with a recycle delay of 100 ms.

All ^{29}Si direct excitation (DE) MAS NMR spectra were recorderd with a Bruker AMX300 spectrometer (7.0 T) on samples packed into 4 mm zirconia rotors spun at 5 kHz, the ^{29}Si resonance frequency being 59.6 MHz. Tetramethylsilane (TMS) was used as chemical shift reference. 4,000 scans were accumulated with an interscan delay of 60 s and a 90° ^{29}Si pulse of 5 μs. All cross polarization (CP) MAS ^{29}Si NMR experiments were performed on a Bruker Avance400 NMR spectrometer, operating at an ^{29}Si NMR frequency of 79.5 MHz. Depending on the sample 5,300, 14,000 or 20,000 scans were accumulated with an interscan delay of 10 s. The duration of the 90° proton pulse was 2.5 μs, and the length of the contact pulse 4 ms.

Catalytic Experiments

In a typical catalytic experiment, 1 g cellulose, 0.5 g Ru/H-USY catalyst (containing 0.2 wt% of Ru) and 50 ml of a 0.96 mM aqueous HCl solution were loaded in a 100 ml stainless steel autoclave (Parr Instruments Co.). The reactor was flushed with N_2 to remove air. The mixture was stirred at 750 rpm and heated to 463 K. Steam pressure in the reactor confirmed that almost all water is present in liquid form.[14] The reactor was then pressurized to 5 MPa with hydrogen. This moment was used as the start of the reaction. Samples taken during reaction were quickly cooled in an ice bath. In case of consecutive runs, no sampling was done during prior runs, avoiding catalyst loss. After each reaction the reactor was cooled and depressurized, samples of the solution were analyzed, while the filtered zeolite catalyst was washed over a Büchner with excess of water. Gravimetric analysis showed no significant catalyst loss during this procedure. After drying in air at 298 K, regenerated catalysts were re-used in a reaction with fresh cellulose.

Sample analysis

After derivatization to the corresponding trimethylsilylethers,[10] reaction product samples were analyzed on a Hewlett Packard 5890 GC equipped with a 50 m CP-Sil-5CB column and a FID detector. In addition, aqueous samples were analyzed by an Agilent 1200 Series HPLC equipped with a Varian Metacarb 67C column (300 x 6.5 mm) and a RI detector, with water as mobile phase. Formation of cello-oligomers was monitored by analysis on a Dionex ICS 3000 HPLC equipped with a CarboPac PA-100 column and pulsed amperometric detection. All

product yields are expressed as C mol% and are calculated as: yield (%) = [moles C in product/total moles C loaded into reactor] x 100. Due to the insoluble nature of cellulose, the conversion of cellulose was determined by dissolved organic carbon analysis of the centrifuged product mixture (dissolution of cellulose), using an Analytik Jena Multi N/C 2100 TOC Analyzer equipped with IR detector.

RESULTS

Physicochemical characterization of H-USY after HLW treatment

For sake of conformity with previous work,[2b] all treatments in HLW in the present study were conducted in aqueous HCl solutions (35 ppm). To clarify the influence of these slightly acidic conditions on the zeolite stability, USY19, USY9 and USY3 were treated in absence and in presence of HCl and characterized (see SI for more details). From this study, it can be concluded that the influence of 35 ppm HCl in HLW on the stability of H-USY zeolites is almost negligible compared to that in HLW water alone. From now on, all treatments in HLW were done in aqueous mmolar solution of HCl and referred to as 'HLW treatment'.

Zeolite dissolution in HLW was monitored by measuring the concentration of Si and Al in the supernatant solution with ICP-AES. Relative amounts of dissolved Si and Al are listed in Table 2 (Table S2 for absolute values).

Table 2. Relative amounts of Si and Al dissolved from H-USY and amorphous silica-alumina during treatment in HLW at 463 K.

Material	Dissolved Si (%)	Dissolved Al (%)
Y25	10.0	1.0
USY19	13.5	< 0.5
USY9	12.0	2.8
USY3	9.4	5.2
Siral30	15.0	< 0.5

Whereas all H-USY zeolites dissolve to some degree under the applied conditions, they show significant Si leaching. Thus, desilication rather than dealumination is the dominant process in liquid water,[8e, 15] in contrast to what occurs in steaming conditions.[5b, 16] From the zeolites, the amount dissolved Si is minimal for Y25 and USY3, while for steam stabilized USY19 this amount is maximal.

Table 2 and Figure S4 further show that the extent of Al dissolution is correlated with increasing initial framework Si/Al ratio. The richer the initial framework in Al, the more stable is framework Al (**FAl**) in HLW. However, USY19 constitutes an exception to this trend: in contrast to Si, its FAl is unexpectedly stable under HLW treatment.

Finally, Siral30, an amorphous silica-alumina with SiO_2/Al_2O_3 molar ratio of 70/30 had highest resistance to Al leaching in HLW, while Si showed the highest lability among the samples used. As Si and Al exist in more or less segregated domains of SiO_2 and Al_2O_3,[17] it is obvious that the low solubility of $Al_xO_yH_z$ in HLW is at the basis of this high resistance to leaching. It is evident that tetrahedral Si in crystalline (zeolite) environment will be more stable, compared to the amorphous environment of Siral30.

Zeolite crystallinity as revealed by powder XRD, is a strong indication of the resistance of the catalyst support to HLW. XRD results (Table 3) (see Figure S5 for diffractograms) confirm the ICP-AES analysis: the higher the Si/Al ratio, the more susceptible USY zeolites are to amorphization in HLW.[8d, 8e, 18] Extensively dealuminated zeolites like USY6 and USY3 are transformed into completely amorphous silica-alumina, characterized by a single broad diffraction band around 22.5 °2θ. USY19 again proves to be the most stable zeolite, with a remaining relative crystallinity of 88 %.

The porosity data of the original zeolite samples prior to HLW treatment are shown in Table 3. Y25 and USY19 have almost no mesopore volume, in contrast with more severely steamed zeolites. All zeolites have a micropore volume around 0.30 mL/g, except for zeolites USY19 and especially USY16. The latter two materials originally did not undergo acid treatment and will retain all EFAl. This has been correlated with partial micropore blockage by EFAl.[19] In HLW, all zeolites were losing most of the micropore volume (Table 3, right data in appropriate column) (Figure S6-a). Only zeolites USY16 and especially USY19 with high amount of EFAl, retained a notable micropore volume. In contrast, mesopore volumes increase in all materials (Figure S6-b). In USY19 and USY16 the increase in mesopore volume even compensates for the microporosity loss, resulting in increased total porosity. After HLW treatment of Y25, a thermally treated NH_4-Y sample (Table 1), microporosity loss is not compensated by mesopore formation, the strongly reduced pore volume pointing to the formation of a dense amorphous material.

The effect of HLW on the zeolite pores can be studied in more detail with electron microscopy. TEM-HAADF experiments were performed on a untreated and a treated USY19. With these experiments the pores can be visualized on a nanoscale.[20] To assess the interconnectivity in both samples, electron tomography was used.[21] In mildly steamed USY zeolites, like USY19, mostly cavities are formed. This is clearly observed in 3D by the electron tomography results (the animated versions of the tomograms of USY19 sample for both before and after treatment in HLW are provided in the supporting information as a video) from the mildly steamed USY zeolite sample (Figure 1-c). Although such cavities are included in the measured mesopore volume, they are only partially connected to the external surface and as such do not significantly impact intracrystalline diffusivity.[19, 22] In Figure 1–b a HAADF-STEM image of USY19 after treatment in HLW is shown. Clearly, treatment in HLW leads to the formation of new mesopores, which is in good agreement with our N_2 physisorption data (Table 3). The same observation is drawn from the electron tomography results (Figure 1-d). Importantly, in mildly steamed zeolites, HLW also leads to the conversion of cavities into large mesopores

connected to the external surface. The size of these pores (> 20 nm, see Figure 1-b, d and S7) implies an enhanced intracrystalline diffusivity for especially large substrates. Thus, mildly steamed H-USY zeolites can be made more accessible for substrates larger than 20 nm through treatment in HLW.

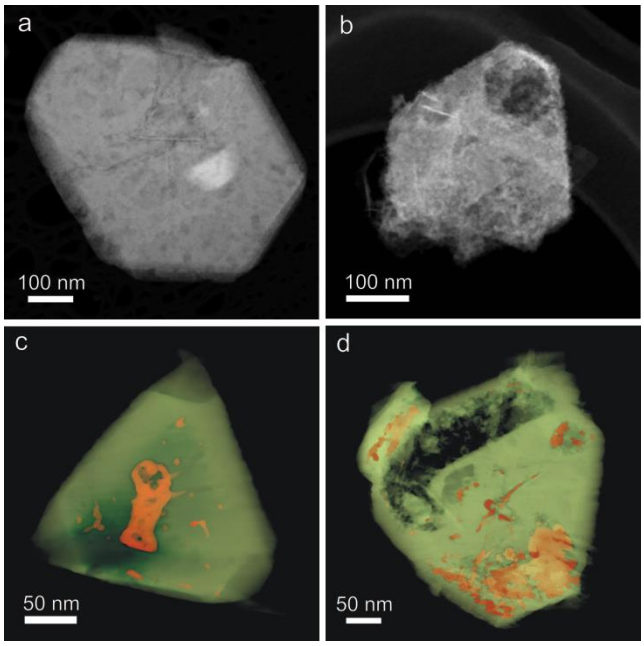

Figure 1. HAADF-STEM images of USY19 (a) before and (b) after treatment in HLW. 3D visualization of the electron tomography reconstructions of zeolitic particles (c) before and (d) after HLW treatment. Note that the mesopores within the particles are visualized in orange.

In Table 3, the Brønsted and Lewis acid site densities as measured by pyridine FTIR are presented for all zeolites studied. The original Brønsted acidity of the zeolites decreases with severity of steaming/acid treatment or framework dealumination. However, for USY16 an unexpectedly low Brønsted acid density is measured (*vide infra*). USY19, USY16 and USY9 have a high concentration of Lewis acid sites, in line with the high amount of EFAl in these materials (Table 4). In HLW, all zeolites lose a significant part of their Brønsted acidity. In addition, Lewis acidity decreases in all materials except for USY6 and USY3, samples subjected to exhaustive acid treatment (Table 1). The relative loss of Brønsted acid sites in steamed zeolites decreases with increasing framework Al T atom fraction (Figure 2). The loss for Y25 is expected, given its extensive structural degradation. However, the relative loss of Lewis acid sites in steamed zeolites increases with increasing framework Al T atom fraction. Despite the extensive loss of Lewis acidity for USY19 and USY16, both samples show a high amount of EFAL(VI) after treatment in HLW (Table 4), which could suggest sintering of the EFAl species, rendering them inaccessible.

Typical ^{27}Al MAS NMR spectra of zeolites before and after HLW treatment are given in Figure 3-a and b. The activated Y25 (Figure 3-a) shows a resonance at 60 ppm arising from Al tetrahedrally coordinated in the faujasite framework (**FAl(IV)**), and around 0 ppm assigned to octahedrally coordinated EFAl.[23] The latter signal is a superposition of a sharp and broad signal, the latter one pointing to the presence of a small amount of oligomeric **EFAl(VI)**, typical in amorphous alumina.[24]

Table 3. Relative XRD crystallinity after treatment in HLW together with porosity and acidity of H-USY zeolites before and after treatment in HLW.

Material	Relative crystallinity after treatment (%)	Porosity before/after treatment			Acid density before/after treatment	
		Micropore volume (mL/g)	Mesopore volume (mL/g)	Total pore volume (mL/g)	Brønsted acidity (µmol/g)	Lewis acidity (µmol/g)
Y25	45	0.31 / 0.03	0.02 / 0.10	0.33 / 0.13	684 / 252	312 / 220
USY19	88	0.27 / 0.16	0.02 / 0.26	0.30 / 0.42	519 / 359	114 / 40
USY16	33	0.22 / 0.07	0.13 / 0.41	0.35 / 0.48	180 / 129	116 / 63
USY9	17	0.29 / 0.04	0.15 / 0.31	0.44 / 0.36	371 / 111	92 / 75
USY6	14	0.30 / 0.04	0.13 / 0.29	0.44 / 0.33	200 / 55	39 / 51
USY3	0	0.31 / 0.01	0.15 / 0.29	0.46 / 0.30	127 / 17	17 / 20

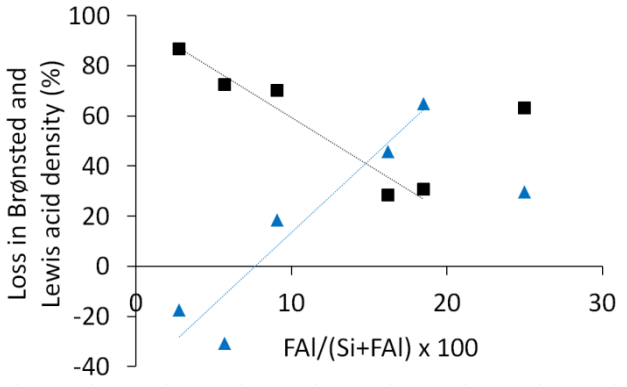

Figure 2. Relative loss in Brønsted (black squares) and Lewis (blue triangles) acid density against framework Al content of H-USY zeolites during treatment in HLW.

The sharp signal at 0 ppm is usually assigned to cationic monomeric EFAl(VI) species on ion exchange positions (**EFAl(I)**).[24] It is not unexpected to see that from USY3, thoroughly acid washed after steaming, almost all EFAl(VI) was removed, only traces of EFAl(I) remaining. This spectrum is very similar to that of Y25 (Figure 3-a), though with less pronounced resonances at 60 ppm and 0 ppm. The spectrum of USY19 (Figure 3-a) also shows resonances at 60 and around 0 ppm, the 0 ppm signals of EFAl(VI) and EFAl(I) being much more prominent, in line with the dealuminating effect of steaming. In addition, a signal at 30 ppm is visible. This signal has been associated with penta-coordinated[5d, 25] or distorted tetrahedrally coordinated Al.[25b, 26] Reflecting the uncertain coordination, this species is denoted as **Al(x)**. No consensus exists whether it belongs to the zeolite framework or not.[8f, 22] The spectra of USY16, USY9 and USY6 (Figure S8), are similar to those in Figure 3-a, with a different distribution of species (Table 4).

To obtain more insight into the nature of the different Al centers in USY19, ^{27}Al MQMAS NMR spectra were recorded (Figure 3-c and d). 2D MQMAS NMR helps to distinguish between the spectral effects of chemical-shift heterogeneity and quadrupolar coupling. In particular, signals of Al species with distorted tetrahedral and penta-coordination, which have similar shift values in 1D ^{27}Al NMR, can be unambiguously assigned. The shape and orientation of the resonances in the 2D spectrum reveal information on the chemical or quadrupolar nature of the underlying broadening. The *higher* the tetrahedral or octahedral symmetry of the oxygen coordination, the weaker the quadrupolar coupling and the *closer* the signals are located to the diagonal of the 2D spectrum. Al atoms with strong quadrupolar coupling resulting from distorted oxygen-coordination symmetry or nearby cations or cationic EFAl species, have elongated lineshapes along the *horizontal* single-quantum shift axis. In contrast, a distribution of chemically different Al states causes the 2D NMR resonances to be smeared out along the *diagonal* direction. Finally, *anti-diagonally* broadened 2D signals are indicative of chemically identical Al distributions with varying distortions in the oxygen coordination.

The MQMAS spectra clearly show two types of tetrahedral Al, T_1 and T_2, and one type of octahedral Al, O_1 (Figure 3-c, Figure S9-a and Table S3). As evident from their resonance position close to the spectrum diagonal, the T_1 and O_1 species have high coordination symmetry and should correspond to FAl(IV) and EFAl(VI), respectively. In contrast, the off-diagonal position and elongated lineshape of the T_2 resonance is typical for tetrahedral Al with distorted coordination symmetry or nearby cationic species. The bimodal T Al distribution, also reflected in the 2D spectrum projection on the (vertical) isotropic shift axis, is typically observed for steam-calcined USY, but not for zeolite Y or for steamed samples subjected to exhaustive acid treatment resulting in a lower EFAl content. No penta-coordinated Al is observed, proving that the Al(x) signal in the 1D ^{27}Al NMR spectra exclusively arises from distorted tetrahedral Al (T_2).

After treatment in HLW, a portion of FAl(IV) is extracted from the framework of Y25 and is converted into EFAl(VI) (Figure 3-b, Table 4, Figure S9-b and Table S3). It should be stressed that the EFAl(I) sharp signal disappears completely in all samples, indicating the instability of this species in HLW. Given its assignment to cationic monomeric EFAl, its exchange for H^+, followed by dissolution or transformation into oligomeric EFAL(VI), is straightforward. The 2D MQMAS spectra of USY19 before and after HLW treatment were deconvoluted[13] (for more details see SI). The obtained line shape parameters and signal heights are listed in Table S3. Before and after HLW treatment the MQMAS line shape of the EFAl(VI) signal reflects a distribution of chemical shifts and quadrupolar coupling constants. Upon HLW treatment the true shift of the EFAl(VI) species changes from 0 to 4 ppm, as can be seen directly in the projections on the isotropic frequency axes in Figure 3-c and d. Such shift change is consistent with an increased amount of O-Al in EFAl species at the external rim of zeolite crystallites. Indeed, the deconvolution data indicate that Al(x) species are transformed into EFAl(VI), while FAl(IV) remains approximately equal (Table 4 and Table S3).

As pointed out before,[27] especially O_1 Al species in USY tend to have lower NMR visibility at intermediate magnetic fields. The intensive contact with water during the HLW treatment may well result in better visible NMR Al. An increase by about 20% of the absolute ^{27}Al NMR intensity of USY19 after HLW treatment is an indication for this.

Table 4. Distribution of different Al species in USY before and after treatment in HLW.

Sample	Before treatment in HLW (%)				After treatment in HLW (%)			
	FAl(IV)	EFAl(IV)	Al(x)	EFAl(VI) + EFAl(I)	FAl(IV)	EFAl(IV)	Al(x)	EFAl(VI) + EFAl(I)
Y25	77	0	0	22	60	0	0	40
USY19	19	0	40	41	20	0	33	47
USY16	23	0	31	46	2	10	15	73

USY9	34	0	24	42	3	26	20	51
USY6	67	0	11	22	1	77	0	22
USY3	65	0	21	15	0	69	0	31

This is more than expected from the 13.5 % leaching of Si (Table 2). For an initial Si/Al ratio of USY19, this would correspond to a 10 % increase of the gravimetric Al content.

Figure 3 suggests that the treatment in HLW leads to the formation of a new Al species in the Al(IV) resonance range (Table 4), its share increasing with the Si/Al ratio of the untreated sample. Because this species dominates the spectrum of the treated USY6, its ^{27}Al MQMAS NMR spectrum will give a good idea about the properties of this species. From the 2D NMR data (Figure S10), it can be derived that the true chemical shift of this species is about 55 ppm. Ravenelle et al. also observed this resonance and assigned it to tetrahedrally coordinated extra-framework Al (**EFAl(IV)**).[8e] From the XRD data (Figure S5), e.g. the diffractogram of USY3 after treatment in HLW, it is concluded that this species is XRD amorphous. In addition, it has been reported that the NMR spectrum of several amorphous silica-alumina materials contain a signal at this position.[17b] Therefore, this new species likely indicates the formation of an amorphous phase, similar to a silica-alumina with low Al content.

The ^{29}Si MAS NMR spectra shown in Figure 4-a are characteristic for USY zeolites, showing signals arising from Si atoms connected to four Si atoms ($Q_{4,ord}$, at -107 ppm), to three Si atoms and one Al atom or hydroxyl group (Q_3, at -102 ppm), to two Si atoms and two Al/OH (Q_2, at -97 ppm) and to one Si atom and three Al/OH (Q_1, at -91 ppm). The last two signals are only clearly present in Y25 and USY19. The broad signal at -111 ppm in the spectrum of USY3 ($Q_{4,desord}$) is indicative of a small amount of amorphous silica[28] or silica-alumina.[24] Following these assignments, HLW treatment clearly induces the formation of an amorphous silica-alumina phase in all zeolites (Figure 4-b). However, the extent to which this happens depends on the Si/Al ratio of the starting material. Y25 forms only a small amount of amorphous material, USY19 remains relatively unaffected, while the spectrum of USY3 is dominated by amorphous material. Furthermore, signals in the spectra of Y25 and USY3 are broadened, a further indication of crystallinity loss.

In Figure 5 FTIR spectra of the OH-region before and after HLW treatment are shown. The FTIR spectrum of Y25 (Figure 5-a) shows a more complex OH stretching spectrum than expected for a so-called HY, with a sharp HF bridged silanol vibration (BSV) around 3640 cm^{-1} (O_1-H in supercages), and a broadened LF BSV centered at 3550 cm^{-1} (O_3-H vibrating in 6-ring).[29] In sample Y25, an enhanced contribution of lattice terminating silanol groups is present at 3745 cm^{-1},[30] while the two types of Brønsted acidic sites found in H-USY zeolites, a HF' and LF' band at 3603 and 3525 cm^{-1}, respectively, are shifted to lower wavenumbers and show reduced intensities.

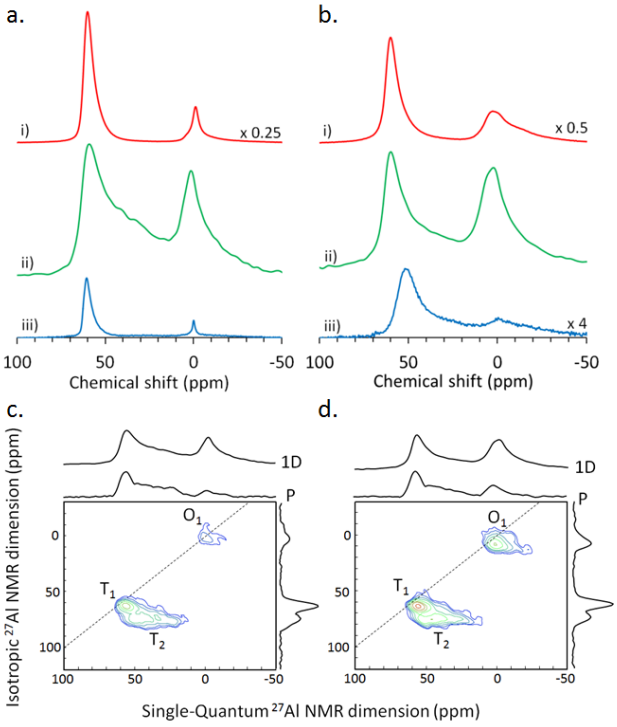

Figure 3. 1D ^{27}Al MAS NMR spectra from (a) untreated and (b) HLW treated i) Y25, ii) USY19 and iii) USY3; ^{27}Al MQMAS NMR spectra of USY19 (c) before and (d) after HLW treatment. Projections P on the single-quantum frequency axis and on the isotropic-frequency axis are shown along the horizontal and vertical axes of each 2D spectrum, respectively. Quantitative 1D ^{27}Al MAS NMR spectra are shown on top of each 2D spectrum for comparison.

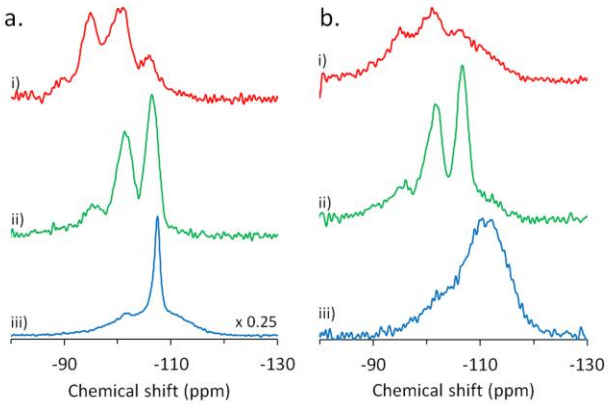

Figure 4. ^{29}Si DE MAS NMR spectra from (a) untreated and (b) HLW treated i) Y25, ii) USY19 and iii) USY3.

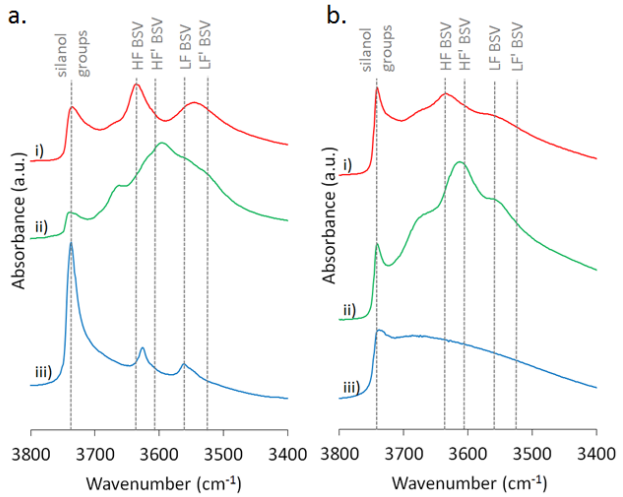

Figure 5. FTIR spectra of degassed i) Y25, ii) USY19 and iii) USY3, before (left) and after (right) treatment in HLW.

Although the HF' band is only partly reactive towards gaseous bases,[29-30] the HF' and LF' bands were assigned to BSVs with enhanced acidity disturbed by neighboring octahedral Al.[5a, 29] The latter species show non-acidic OH stretching vibrations at 3680 and 3600 cm^{-1} (the non-acidic part).[5a, 29-30] Clearly, Y25 shows features of HY and H-USY. The high concentration of EFAl in USY19 (Table 4) gives rise to a more important contribution of the 3680, 3603 and 3520 cm^{-1} bands (Figure 5-a). The FTIR spectrum of USY3 (Figure 5-a) contains only the HF, LF and silanol bands. During severe steaming, a large amount of silanol groups is created by dealumination, leading to an intense contribution of the 3750 cm^{-1} band. UYS3 contains almost no EFAl (Table 4), hence HF' nor LF' bands were observed.

After HLW treatment, the OH stretching region in the spectrum of USY19 (Figure 5-b) shows increased share of silanol groups, with the typical features assigned to EFAL species still visible. This is in line with the observed desilication of the zeolites, involving hydrolysis of a Si-O-Si bond resulting in formation of two silanol groups.[31] In accordance with the acid density data (see Table 3), USY19 retains a noticeable part of its acidity. This is in contrast with the almost complete disappearance of bands attributed to acidic groups in USY3 (Figure 5-b). The broad almost structureless OH band is typical for hydrogen bonding in amorphous silica.[32] In particular, signals have been associated with non-structural Al-OH groups originating from partially hydroxylated EFAl or silanol groups at defect sites.[29-30, 32-33] The spectrum of Y25 (Figure 5-b) also shows a less structured spectrum with enhanced amount of silanol groups.

Typical vibration bands of H-USY samples disappear in the framework vibrational spectrum of USY3 after treatment in HLW (Figure S11), while they remain visible in the spectra of Y25 and USY19 (Figure S11). The disappearance of such bands is indicative for the transformation of the zeolitic material to an amorphous silica-alumina (see supporting information for more details). These observations are in agreement with the other characterization data, showing loss of zeolitic properties in Al-deficient zeolites upon HLW treatment.

In time stability of USY19 in HLW

Up to this point, stability of H-USY zeolites in HLW was studied for a period of 24 h. The results clearly define USY19 as the most stable H-USY zeolite in HLW. Long-term effects in HLW up to 120 h on this material are now reported.

Table 5 shows Si and Al dissolution from USY19 after increasing times in HLW (Figure S12 and Table S4). Al dissolution does not exceed 0.5 % after 120 h. Si dissolution levels off after the initial treatment of 24 h, indicating a gradual stabilization of USY19 after the initial 24 h. The micropore volume of USY19 further decreases after 24 h treatment, albeit at a reduced pace (Table 5). Mesopore volume reaches a maximum after 24 h of treatment and then decreases.

Figure 6–a (and Table S5) report the acid density of USY19 against time after treatment in HLW. Interestingly, Brønsted acid density increases during the first 10 h in HLW. This can be caused by a better accessibility of the acid sites for the pyridine probe molecule due to the increased pore volume and by an exchange of charge compensating Al cations, e.g. EFAl(I), for protons. After the initial increase, Brønsted acidity starts to decrease. However, after 24 h of treatment, this decrease slows down considerably, once more pointing to a gradual stabilization of the material after an initial period of more intense transformations.

The Lewis acidity showing an increase during the first 5 h, afterwards decreases gradually up to 24 h of treatment. This cannot be correlated with an increased solubility of $Al_xO_yH_z$ species as almost no dissolved Al could be detected (Table 2), a relationship with enhanced sintering of such species being obvious. After the initial 24 h, the amount of Lewis acidity stabilizes. Detailed changes of the concentration of the individual Al sites (Figure 6-b) were obtained from the deconvolution of ^{27}Al MAS NMR spectra of USY19 (Figure S13). The figure shows other evidence for gradual stabilization of USY19 during HLW treatment. The change in concentration of the different Al species shows that during the first 24 h, part of the dangling Al (Al(x)) disappears at the expense of freshly formed EFAl(VI), while the concentration of FAl(IV) remains approximately equal. During the next 96 h of HLW treatment, the share of FAl(IV) still remains fairly constant, while Al(x) decreases only slightly. From the ^{27}Al MQMAS NMR spectrum of a long-treated USY19 (Figure S13 and Table S6), it can be concluded that the T_1 and T_2 line shape parameters are conserved even after 120 h treatment. During the first 24 h the true shift of the O_1 Al species changes from 0 to 4 ppm, which is further moved to 8 ppm after 120 h of treatment, indicative of an increased amount of EFAl species at the external rim of the zeolite crystallites. A comparison of this 2D Al NMR spectrum with that of USY6 after 24h treatment (Figure S10) clearly shows that even at longer treatment times EFAl(IV) formation is absent in Al-rich USY zeolites. The ^{29}Si MAS NMR and ^{29}Si CP MAS NMR spectra nor the IR

framework vibrations show major changes after 120 h treatment (see SI).

As expected from these results, XRD diffractograms of USY19 after 10, 24 and 120 h treatment in HLW (Figure S16) show only minor differences. While there is a modest increase in the amount of amorphous material during the final 96 h treatment, the samples remain highly crystalline (70 % of the initial crystallinity compared to 88 % after 24 h). Interestingly, the diffractogram of USY19 after 120 h treatment in HLW shows three new reflections emerging at 12, 14 and 25 °2θ, caused by the formation of a new crystalline phase or by a regular breakdown of the framework.

Summarizing, HLW treatment only significantly affects the characteristics of USY19 during the initial 24 h in HLW. Afterwards, the material shows a gradual stabilization, retaining much of its zeolitic characteristics, in contrast to what is observed for more siliceous H-USY zeolites.

Table 5. Relative amount of Si and Al dissolution and change in porosity and acid density of USY19 after treatment in HLW.

Treatment time (h)	Dissolution material		Pore volume		
	Si (%)	Al (%)	Micropore volume (mL/g)	Mesopore volume (mL/g)	Total pore volume (mL/g)
0	/	/	0.27	0.02	0.30
10	8.8	< 0.5	0.23	0.08	0.31
24	13.5	< 0.5	0.16	0.26	0.42
120	16.7	< 0.5	0.09	0.14	0.23

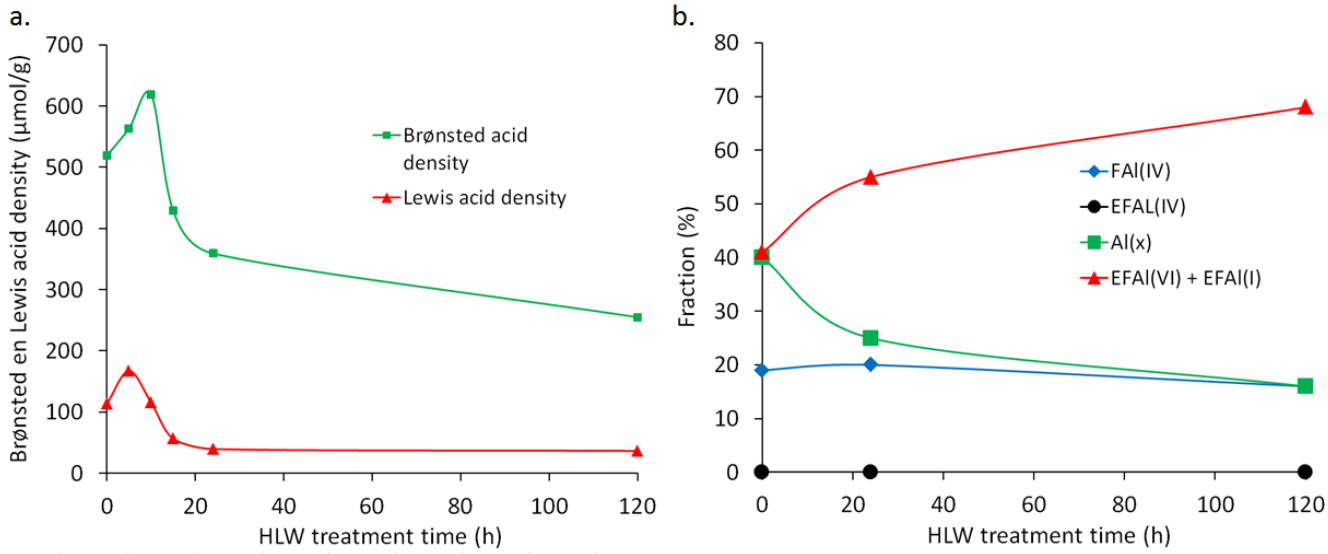

Figure 6. In time stability of USY19 in HLW: (a) change of Brønsted and Lewis acid density of USY19 during treatment in HLW; (b) change of Al species in USY19 in HLW.

Influence of EFAl on the physicochemical properties of H-USY

It is known from literature that EFAl, formed during steaming of Y zeolite, is deposited preferably on the outer surface and in the mesopores.[19] In addition, the porosity and acidity data (Table 3) seem to imply that zeolites with a high amount of EFAl have a significantly lower micropore volume and (in the case of USY16) a lower Brønsted acidity than expected.

To investigate the influence of EFAl species on the physicochemical chemistry, a USY16 sample was slurried for 30 minutes with a 10 % ammonium acetate solution at a pH of 3 according to a previously reported Al leaching procedure.[5d] The Si/FAl ratio of this sample, denoted as USY16$_w$, increased from 5.9 to 9.9 by this treatment. ^{27}Al MAS NMR data (Figure S17 and Table S7) show that about 62 % of all EFAl species are removed from the zeolite, leading to an increased micropore and mesopore volume (Table S8). Even though large amounts of acidity generating Al species, FAl(IV) and Al(x) (*vide infra*) are leached, the Brønsted acid density of USY16$_w$ is 48 % higher than that of USY16 (Table S8).

From the ICP data, it is obvious that desilication is the dominant phenomenon during HLW treatment as almost no Al leaching was measured. In contrast, the ^{27}Al MQMAS NMR data suggest that there is an increase of non-framework Al species at the external rim of zeolite crystallites. To study a possible local enrichment of Al, EDX accompanied with HAADF-STEM was performed on a USY19 before and after 24 h HLW treatment (Figure 7-a-j). The HAADF-STEM image of USY19 after treatment in HLW (Figure 7-f) shows the formation of several lamellar species at the outer surface of the zeolite. From the STEM-EDX measurements it is seen that these species are richer in Al than in Si when compared to the chemical composition of USY19 before treatment (Figure 7-b, d, g and i), indicating that HLW, as does steaming, induces

the formation of Al-rich species at the outer surface / external rim of the crystallites.

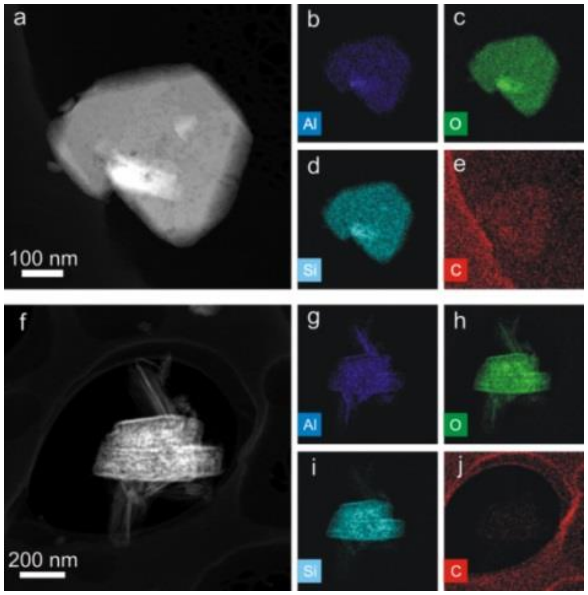

Figure 7. HAADF-STEM images from USY19 (a) before and (f) after 24 h treatment with STEM-EDX chemical maps for Al-K, Si-K, O-K, and C-K from the same area.

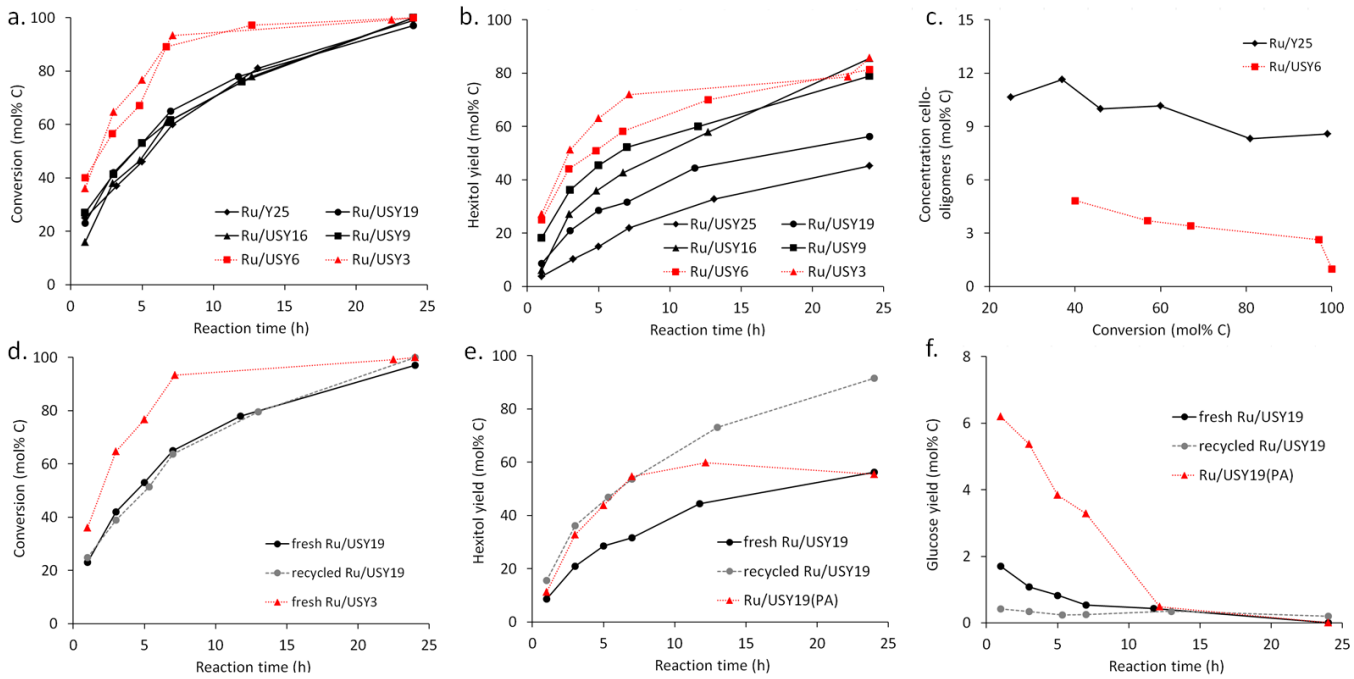

Figure 8. Cellulose conversion at 463 K and 5 MPa H_2 pressure with 0.2 wt% Ru on H-USY zeolites (a); hexitols yield (b); concentration of cello-oligomers against cellulose conversion (c); cellulose conversion over fresh and recycled Ru/USY19 and fresh Ru/USY3 (d); hexitol yield over fresh and recycled Ru/USY19 and Ru/USY19(PA) (e); and glucose formation over fresh and recycled Ru/USY19 and Ru/USY19(PA) (f).

Catalytic performance of freshly activated Ru/H-USY in hydrolytic hydrogenation of cellulose

The implication of the reported physicochemical changes of H-USY and supported Ru in HLW, mimicking the catalytic conditions, will be evident from the experiments with these catalysts in the hydrolytic hydrogenation of cellulose, subsequently involving (i) hydrolysis of insoluble cellulose into soluble cello-oligomers by HCl and HLW, with a possible contribution of external zeolite acid sites (*vide infra*), (ii) hydrolysis of cello-oligomers to glucose by zeolitic acid sites in the meso- and micropores, and (iii) hydrogenation of glucose to sugar alcohols or hexitols by ruthenium nanoparticles located in the zeolite micropores, including sorbitan from acid dehydration of sugar alcohols.[2b, 34]

Figure 8-a illustrates cellulose conversion against reaction time, as measured by cellulose solubilization, in presence of different Ru/H-USY catalysts. It appears that with all catalysts cellulose can be fully converted. This seems to occur more rapidly with Ru/USY6 and Ru/USY3. Figure 8-b shows that the rate of hexitol formation increases in the following series of catalysts: Ru/Y25 < Ru/USY19 < Ru/USY16 < Ru/USY9 < Ru/USY6 < Ru/USY3. Thus, the rate of hexitol formation is correlated with the degree of zeolite dealumination. As a direct consequence of the results of Figure 8-a and b, hexitol selectivity with Ru/H-USY catalysts amounts to two levels, the higher one for the more extensively dealuminated zeolites (Figure S19). Figure 8-c shows the concentration of soluble cello-oligomers ($1 < DP < 8$) against cellulose conversion for fresh Ru/Y25 and Ru/USY6, catalysts with low and high hexitol selectivity, respectively. For all cellulose conversions, the concentration of cello-oligomers is significantly lower with Ru/USY6, an extensively dealuminated zeolite.

Catalytic performance of recycled Ru/H-USY catalysts

As the physicochemical and catalytic studies were carried out in identical conditions, the influence of the observed physicochemical transformations on catalyst performance can be assessed by recycling the catalysts and re-using them with fresh cellulose.

Table 6 compares hexitol yields for fresh and recycled Ru/H-USY catalysts. The results after 7 h reaction time are taken as a measure for the rate of hexitol formation, while results after 24 h reaction reflect hexitol yield at full conversion. Only Ru/USY3 shows significantly reduced hexitol formation. Surprisingly, rate and yield of hexitol formation over mildly dealuminated zeolites (USY19, USY16 and USY9) is markedly increased, with Ru/USY19 and Ru/USY9 reaching a final yield of over 90 %. The enhanced yield is not caused by a higher activity but by a higher selectivity. Figure 8-d compares the cellulose conversion of a fresh Ru/USY19 and Ru/USY3 catalysts with a low and a high rate of cellulose conversion, respectively, and a recycled Ru/USY19. Although the higher yields were obtained by the recycled Ru/USY19, Figure 8-d shows similar cellulose conversions against reaction time with fresh and recycled Ru/USY19.

Long-term catalytic performance of Ru/USY19

In addition, long-term stability was studied for Ru/USY19, pre-aged (**PA;** 120 h treatment in HLW) prior to a catalytic test. Figure 8-e compares the hexitol yield with Ru/USY19(PA), as well as with fresh and recycled Ru/USY19. The freshly prepared and activated catalyst (Ru/USY19) shows a reduced rate of hexitol formation compared to its recycled form. In the first stages of the reaction, performance of Ru/USY19(PA) parallels that of the recycled catalyst. In later stages, however, hexitol production levels off leading to a final yield comparable to that obtained over fresh Ru/USY19. It should be noted that during the reaction with Ru/USY19(PA), higher glucose concentrations are found in the mixture than in any other reaction in this study (Figure 8-f). This is a clear indication of a loss of hydrogenation activity of the catalysts. To investigate the behavior of the hydrogenation catalyst (the supported ruthenium particles), a Ru loaded USY 19 was treated for 120 h in HLW. After this treatment a marked decrease in ruthenium dispersion (from about 12 to a few %) is observed (Figure S18) which confirmed the abovementioned loss of hydrogenation activity in the catalytic data. Alternatively, a USY19(PA) zeolite, showing enhanced stability in HLW (*vide supra*), was loaded with Ru and activated. This Ru/USY19(PA) catalyst in HLW, though initially showing 30 % Ru dispersion, exhibited a drastically reduced dispersion to a few % after 24 h in HLW(Figure S18). This indicates that Ru sintering and decay of the zeolite framework do not necessarily change in parallel.

Table 6. Comparison of hexitol yields over fresh and recycled Ru/H-USY catalysts.

Catalyst	Hexitol yield over fresh / recycled catalyst (mol% C)	
	7h	24h
Ru/Y25	22 / 17	45 / 45
Ru/USY19	32 / 54	56 / 92
Ru/USY16	43 / 51	86 / 78
Ru/USY9	52 / 74	79 / 95
Ru/USY6	58 / 53	81 / 87
Ru/USY3	72 / 11	86 / 22

DISCUSSION

This contribution aims at investigating the stability of H-USY zeolites in HLW against fundamental properties related to composition. Hence, it is important to know which Al species are part of the FAU framework, and thus generates acidity. However, since no general agreement exists on the framework or extra-framework location of the 30 ppm Al species (Al(x)) in ^{27}Al MAS NMR, this matter is addressed first.

Properties of Al(x)

From the ^{27}Al MQMAS NMR results it follows that Al(x) shows resonance in the Al(IV) region, entailing a tetrahedrally coordinated environment, in line with earlier work.[25b, 26] To determine whether Al(x) belongs to the zeolite framework, two sets of Si/FAl ratios were derived, using the bulk Si/Al ratio determined by ICP-AES, corrected with appropriate data from the ^{27}Al MAS NMR spectra, considering as FAl either the 60 ppm signal alone or the sum of the 60 and 30 ppm signals. Agreement of one of these ratios with an independently determined Si/FAl ratio will allow to decide on the nature of Al(x). The Si/Al ratio derived from ^{29}Si MAS NMR constitutes such an independent measurement.[35] The three sets of Si/FAl ratios thus obtained, are shown in Table 7. As all suited materials should be sufficiently rich in Al to allow accurate determination of Si/FAl via ^{29}Si MAS NMR and possess a large amount of Al(x) to provide clear conclusions, only USY19 and USY16 qualify.

Table 7. Comparison of Si/FAl derived from 29Si MAS NMR and from ICP + 27Al MAS NMR.

Zeolite	Si/FAl from	Si/[FAl(IV)]	Si/[FAl(IV) +

	^{29}SiNMR		Al(x)]
USY19	4.7	7.1	4.6
USY16	6.9	9.9	5.4

Considering that ^{29}Si MAS NMR may overestimate Si/FAl ratios,[36] there is acceptable agreement between the ratios when it is assumed that both FAl(IV) and Al(x) are framework constituents. Therefore, Al(x) species, as done previously,[11] are considered behaving as distorted FAl. This entails that both species in the bimodal T Al distribution in ^{27}Al MQMAS NMR (*vide supra*) reflects FAl, most likely without (Al T_1) and with (Al T_2) (cationic) EFAl in the environment. Although their apparent chemical shifts along the single-quantum frequency axis are different, the true chemical shifts (i.e. corrected for the quadrupolar induced shift) of T_1 and T_2 are exactly equal, 61 ppm (see Figure 3 and Table S3). Again a strong indication that both T Al species belong to the zeolite lattice, but differ in the degree of coordination symmetry.

Influence of dealumination on acid site density of H-USY zeolites

Characterization of H-USY by ^{27}Al MAS NMR shows significant changes in the nature and distribution of Al species by treatment in HLW (Figure 3, Table 4). Especially in USY19 and USY16, large amounts of EFAl(VI) are formed. In this section, the influence of EFAl(VI) on zeolite acidity is discussed.

The acidity data in Table 3 show an unexpectedly low Brønsted acid density for USY16, the material with the highest concentration of EFAl (Table 4). It has been shown that EFAl is deposited on the external surface and in the mesopores of the zeolite. In the case of zeolites containing a high concentration of EFAl, it is even deposited in the micropores.[19, 37] This is reflected by the lower micropore volume of USY19 and USY16 (Table 3).

To check whether a high concentration of EFAl could lead to occlusion of Brønsted acid sites, Table 8 compares the measured Brønsted acid site densities via pyridine sorption, with those expected based on Si/FAl ratios including Al(x), and correcting for EFAl(I) and residual Na. From literature it is known that there is a discrepancy between the measured Brønsted acidity and the theoretical value due to the bulky size of the pyridine molecules in contrast to the small size of the pores.[38] Although the twelve membered rings of FAU zeolites should be accessible for pyridine, it is much more difficult to probe the acid sites localized in the smaller sodalite cages. This is reflected by the difference (70 to 75 %) between the theoretical and measured Brønsted acidity. However, the data also indicate that zeolites with a high EFAl content (USY19, USY16) show a much higher difference. Removal of EFAl through acid washing seems to regenerate such occluded sites, as acid washed zeolites (USY9, USY6 and USY3) show a much lower difference between theoretical and measured acid density. The behavior of USY16(PA), showing increased porosity and Brønsted acid site density, further supports this (*vide supra*). This confirms that Brønsted acid sites in USY16 zeolite become inaccessible to the pyridine probe molecule when a high concentration of EFAl is present. The implications for catalysis will be discussed below.

Stability of H-USY zeolites in HLW

Effects of Si and Al dissolution on the physicochemical changes of H-USY zeolites were shown (*vide supra*). The solubility of the two elements has been studied extensively: while Si is only slightly soluble in the 0-9 pH range,[39] above pH 9 there is a strong increase in solubility.[31a] In contrast, Al is poorly soluble in pure water and only slightly soluble in alkali,[40] its solubility reaching its maximum below pH 4.[41]

The Si and Al dissolution data in absence and presence of HCl (see SI) indicate that the solubility rules also dissolution of Al and Si from a zeolite framework. They have been exploited in the design of highly porous hierarchical zeolites with attractive catalytic properties. By treating the zeolites in an alkaline medium, both Si and Al are removed from the zeolite framework,[42] forming intracrystalline mesoporosity.[43]

Table 8. Comparison of expected and measured Brønsted acid densities.

Zeolite	EFAl(VI) content (%)	Brønsted acid density (μmol/g)		Difference (%)
		Expected[a]	Measured[b]	
Y25[c]	0	3843	982	74
USY19	37	2864	519	81
USY16	45	2502	180	93
USY9	20	1475	371	76
USY6	20	733	200	73
USY3	12	458	127	72

[a] From Si/FAl including Al(x) and corrected for EFAl(I) and residual Na; [b] from FTIR of adsorbed pyridine; [c] data for a commercial Y25.

For MFI zeolites, it was observed that, in contrast to the leached silicates, extracted Al species are immediately realuminated on the external surface of the zeolite, exercising a regulatory effect on the dissolution process.[43a, 43b, 44] In the case of Y zeolites (Si/Al = 3 – 6), the high Al content was reported to cause a higher resistance in alkaline media compared to their more Al-deficient (Si/Al > 15) USY analogues.[45] Hereby, the long-range order and Brønsted acid site density of the starting material mostly can be preserved.[44-45]

Up to now, desilication was suggested as the main phenomenon in HLW.[8e] The present data prove that desilication is indeed the main mechanism affecting zeolites in HLW. Solubilization of the framework can be counteracted by the presence of Al in the framework. This can be rationalized by the repulsion of hydroxide anions,

the active species in desilication, by the negatively charged framework containing FAl.[8c, 46] The stabilizing effect of FAl is apparent from the resistance in HLW to degradation of Al-rich zeolites. Therefore, together with topology effects, the Si/FAl ratio is the main factor determining zeolite stability in HLW. As high concentrations of FAl can preserve the key properties of a zeolite, its stability in HLW, in contrast to what can intuitively be expected, resembles more that of zeolites in aqueous bases than in water vapor (steam).

Interestingly, although Y25 has the lowest Si/FAl ratio of all studied zeolites, USY19 and perhaps also USY16 exhibit even higher stability in HLW (Figure 2, Figure 4-b, Figure 5, S4, S5, S6-a and S9). Treatment of Siral30 pointed to the superior stability of amorphous polymeric alumina in HLW, compared to tetrahedrally coordinated FAl (Table 2), in line with the low water solubility of alumina gel.[40-41] Indeed, only USY19, with a high concentration of octahedral EFAl, thought to be similar to oligomeric alumina, shows comparable high Al stability. Therefore, the unexpected high stability of USY19 and USY16 is attributed to the high concentration of EFAl(VI) present. EFAl(VI) is deposited predominantly on the external crystal surface and in the mesopores during steaming[16a, 19] forming a poorly soluble coating around the zeolite crystals, thus protecting the less stable zeolite framework from the hydrolytic action of water. Since USY19 and USY16 contain a high amount of EFAl(VI), they are more stable in HLW than Y25, almost devoid of any EFAl(VI).

Summarizing, the stability of H-USY zeolites in HLW is governed by two main parameters, *viz.* the framework Si/Al ratio and EFAl(VI) content. In neutral and slightly acidic HLW, FAl is more stable than framework Si allowing FAl to protect his own and adjacent framework bonds against hydrolysis. This explains why Al-rich USY zeolites are more stable in HLW. In addition, EFAl(VI) species are less susceptible to hydrolytic attack than the zeolite framework. Moreover, the framework of a USY-zeolite containing a high amount of EFAl(VI) at the external surface is protected against solubilization by the poorly soluble EFAl-layer.

HLW treatment affects the characteristics of USY19 to a limited extent during the initial 24 h. During this period, the initially unstable material transforms into a derivative of USY19 with enhanced stability, retaining much of its original zeolitic characteristics. Moreover, during the initial modification period, cavities that were formed by steaming are converted into large mesopores connected to the external surface, thus showing enhanced accessibility for larger substrates than the untreated zeolite. The implications on catalysis will be discussed below.

These results can stand further generalization. With ^{27}Al MAS NMR, it was shown that treatment in HLW leads to formation EFAl(VI) species(Table 4), being much less soluble in HLW than the zeolite framework itself. Hence, zeolites sufficiently rich in FAl, but initially devoid of EFAl(VI), are expected to self-stabilize over time through formation of a protective Al_2O_3 layer. In Al-poor USY zeolites with no EFAl(VI), there is insufficient Al to form an adequate Al_2O_3 overlayer. Therefore, a 'critical' bulk Si/Al ratio should exist for FAU zeolites, depending on temperature and pH. With lower ratios, zeolites will self-stabilize over time, while with higher values, they will be transformed in a non-acidic, non-microporous, amorphous silica-alumina. The present results point to the existence of a critical Si/Al ratio of around 3 (USY19), which is close to the Si/Al ratio of H-Y (2.6).

Because of the key role of Al in zeolite stabilization in HLW, strongly acidic conditions should be avoided. The fundamental nature of the parameters involved, *viz.* Si and Al water solubility, suggests that the proposed concepts should be applicable to other zeolite topologies as well, though it recently was suggested this might require individual assessment.[8d]

Catalytic performance of Ru/H-USY in HLW

This issue is of increasing importance in view of the recent successful application of zeolites in biomass conversion processes taking place in HLW.[2]

The rate of cellulose conversion to soluble oligomers with Ru/H-USY determines efficient (USY6, USY3) and less efficient catalysts (Y25, USY19, USY16, and USY9). Hence, the observed dependence of cellulose conversion rate on the zeolite catalyst points to an active role of the zeolite in cellulose solubilization, at least for the more active catalysts. Given the cellulose particle sizes (20-50 μm), such interactions should predominantly take place at the external surface of the zeolite crystals. As the cellulose particles decrease in size during conversion, at a certain moment zeolite mesopores may also intervene. This assumption implies that only microporous zeolites devoid of mesoporous like Y25 and USY19 (Table 3) would be slow in catalyzing cellulose hydrolysis, in contradiction with the present data. However, conversion of cellulose into soluble oligomers proceeding through hydrolysis of β-1,4-glycosidic bonds, is catalyzed by Brønsted acid sites. As large amounts of EFAl can block Brønsted acid sites especially on the external surface and in the mesopores (*vide supra*),[19, 37] enhancement of cellulose conversion rate should only be observed for zeolites with a large mesopore volume free of EFAl (USY6 and USY3) (Figure 8–a and Figure 8–d). While recycled Ru/USY19 has a higher mesopore volume than fresh Ru/USY19 (Table 3), it contains a large amount of EFAl(VI) (Table 4). Hence, the added available catalytic surface does not lead to higher activity. A fresh Ru/USY3 catalyst, with only half of the mesopore volume of recycled Ru/USY19, but free of EFAl(VI), shows enhanced cellulose hydrolysis.

Summarizing, solid catalysts with an extensive mesopore network could be effective catalysts in the conversion of cellulose, provided they are free of EFAl. Therefore, dealumination in reaction conditions should be avoided. This imposes a limit on the severity of the applied conditions with respect to reaction temperature and pH. Since Al-containing MFI and MOR zeolites have been shown to be very stable in HLW,[8c] these materials may be better suited for reactions involving large substrates in HLW.

Conversely, hexitol yield and selectivity over fresh Ru/H-USY catalysts show a positive correlation with the

framework Si/Al ratio of the zeolite (Figure 8–b and S19). This trend must be rooted either in (1) the rate-limiting hydrolysis of oligomers to glucose, (2) hydrogenation of glucose to hexitols, or (3) formation of byproducts. Byproducts in these reactions stem from Ru-catalyzed hydrogenolysis, producing C2-C6 products with varying degrees of hydroxylation.[2b] As formation of these products is negligible, hydrogenolysis cannot rationalize the observed selectivity trend. Alternatively, a lack of sufficient hydrogenation capacity would lead to a build-up of glucose, susceptible to temperature-induced degradation reactions.[10] However, almost no glucose or degradation products are encountered. Therefore, hydrogenation cannot be rate-determining and also not explain the differences in hexitol selectivity. Hence, rate-limiting hydrolysis of soluble oligomers into glucose most likely causes the observed trend in hexitol selectivity. From Figure 8-c, it seems that the rate of cello-oligomer hydrolysis to glucose over zeolite catalysts increases with zeolite dealumination. This phenomenon is rooted in the different influences incurred by different degrees of steaming. In mildly steamed H-USY zeolites, mostly cavities are formed.[19, 22] Although they are included in the measured mesopore volume, they are not connected to the external surface and as such do not significantly impact intracrystalline diffusivity. In more severely steamed zeolites, these cavities are connected to each other and to the external surface, forming true mesopores improving intracrystalline diffusivity.[19, 22] In the case of hydrolytic hydrogenation of cellulose, this results in an enhanced rate of cello-oligomer hydrolysis for more severely steamed zeolites. With hexitol formation rate as a measure of cello-oligomer hydrolysis rate, this trend is illustrated in Figure 9, reflecting the higher number of acid sites accessible to large substrates like cello-oligomers.

Figure 9 also shows hexitol formation rates over recycled Ru/H-USY catalysts. In some cases, the difference between the rate of hexitol formation over the fresh and the recycled catalyst is striking. This is again explained by the rate of cello-oligomer hydrolysis. While the performance of Y25 and USY6 remains fairly constant, USY3 has lost almost all activity during the second reaction due a complete loss of zeolitic properties (*vide supra*). In contrast, mildly steamed zeolites (USY19, USY16 and USY9) show increased performance after recycling, due to the higher accessibility of large substrates generated through treatment in HLW (*vide supra*). Thanks to this effect, the performance of mildly steamed zeolites drastically improves through HLW treatment. Hence, hexitol yields up to 95 % can be obtained for recycled catalysts (Figure 8-e).

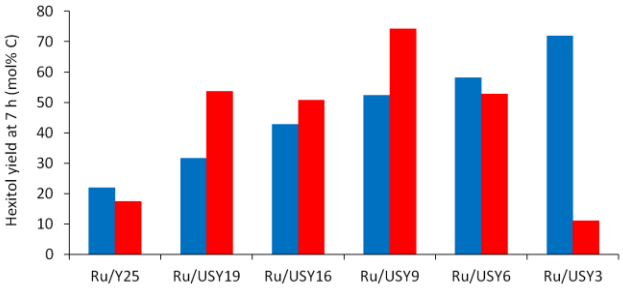

Figure 9. Hexitol yield after 7 h with fresh (blue) and recycled (red) Ru/H-USY catalysts.

CONCLUSIONS

The stability of zeolites in HLW becomes increasingly important in view of the current focus on aqueous processes for biomass transformations. While some dense topologies like MFI and MOR have been shown to be stable at temperatures in excess of 473 K, zeolite Y is known to undergo extensive transformations.[8d] However, the reasons for its relative instability, viz. large three-dimensional pores and an exceptionally large void volume, make zeolite Y an attractive catalyst for biomass conversions. In this study, the fate of commercial H-Y and H-USY zeolites in HLW is assessed against fundamental properties. The findings were related to the performance of bifunctional Ru-loaded zeolite catalysts in the hydrolytic hydrogenation of cellulose.

It was shown that commercial (US)Y-zeolites can be stable in HLW. The stability depends on the different solubility of Si and Al in the material. For USY zeolites in neutral or slightly acidified HLW, desilication was determined to be the dominant mechanism affecting the zeolite framework. The zeolite framework is protected from hydrolysis by FAl species. This accounts for the observed positive correlation between framework Al and framework stability in HLW, opposite to that found under steaming conditions. The stabilizing effect of FAl appears to such extent that Al-rich zeolites are only slightly degraded. In addition, the presence of octahedral EFAl species at the external surface, formed either by steaming or treatment in HLW, further stabilizes the USY due to its very low water solubility. As a result, a mildly steamed Y zeolite containing a large amount of both octahedral EFAl and tetrahedral framework Al is found to exhibit optimum HLW stability. After an initial transformation phase, during which the accessibility of the catalytic active sites are extensively enhanced, the material is self-stabilized for at least five days in HLW. Hence, a critical Si/Al ratio was determined whereby zeolites having a lower Si/Al will self-stabilize over time.

Ruthenium particles on zeolite support were shown to sinter under the applied conditions, reduced metal dispersion leading to decreased catalytic performance in cellulose hydrolysis. More research is needed to assess the sintering susceptibility of other noble metals or multimetallic particles in HLW.

Indirect evidence could be provided for the catalytic role in the conversion of cellulose of solid-solid interactions between substrate and zeolite. Occlusion of acid sites in inaccessible environment by EFAl deposition

may deactivate the catalyst. On the other hand, conversion of smaller substrates, *viz.* cellulose hydrolysis products, that are able to interact with acid sites in the zeolite micropores/pore mouths is promising. Due to the initial transformation phase of the USY zeolites in HLW, an enhanced catalytic surface appears, considerably improving catalyst performance.

ASSOCIATED CONTENT

Supporting Information

The animated versions of the tomograms of the USY19 samples, additional information about catalyst preparation and characterization, a study about the influence of HCl in HLW on the physicochemical properties of H-USY and seven additional tables and sixteen additional figures. This material is available free of charge via the Internet at http://pubs.acs.org.

AUTHOR INFORMATION

Corresponding Author

* E-mail: bert.sels@biw.kuleuven.be, Tel.: +32 16 321610, Fax: +32 16 321998

§ T. Ennaert en J. Geboers contributed equally to this work.

ACKNOWLEDGEMENTS

This work was performed in the framework of IAP (Belspo). T.E. thanks IWT-Vlaanderen for a doctoral fellowship. The authors are grateful to Johan Martens for general financial support through Methusalem, Walter Vermandel, Iris Cuppens and Emmie Dornez for respectively CO chemisorption, ICP and HPAEC analysis, Francis Taulelle for his assistance with the interpretation of the NMR experiments, Danny Verboekend for the well-grounded advice and Filip Boeckx for his work done in the lab. S.B. and G.V.T. acknowledge the European Research Council for funding under the European Union's Seventh Framework ERC grant agreement n° 246791-COUNTATOMS and n° 335078-COLOURATOM.

REFERENCES

(1) (a) Geboers, J.; Van de Vyver, S.; Ooms, R.; Op de Beeck, B.; Jacobs, P. A.; Sels, B. F., *Catal. Sci. Technol.*, **2011**, *1*, 714; (b) Huber, G. W.; Iborra, S.; Corma, A., *Chem. Rev.*, **2006**, *106*, 4044; (c) Kobayashi, H.; Ohta, H.; Fukuoka, A., *Catal. Sci. Technol.*, **2012**, *2*, 869; (d) Murat Sen, S.; Henao, C. A.; Braden, D. J.; Dumesic, J. A.; Maravelias, C. T., *Chem. Eng. Sci.*, **2012**, *67*, 57; (e) Reyes-Luyanda, D.; Flores-Cruz, J.; Morales-Pérez, P.; Encarnación-Gómez, L.; Shi, F.; Voyles, P.; Cardona-Martínez, N., *Top. Catal.*, **2012**, 55, 148; (f) Rinaldi, R.; Schüth, F., *ChemSusChem*, **2009**, *2*, 1096; (g) Simonetti, D. A.; Dumesic, J. A., *Catal. Rev.*, **2009**, *51*, 441; (h) Van de Vyver, S.; Geboers, J.; Jacobs, P. A.; Sels, B. F., *ChemCatChem*, **2011**, *3*, 82.

(2) (a) D'Hondt, E.; Van de Vyver, S.; Sels, B. F.; Jacobs, P. A., *Chem. Commun.*, **2008**, 6011; (b) Geboers, J.; Van de Vyver, S.; Carpentier, K.; Jacobs, P.; Sels, B., *Chem. Commun.*, **2011**, *47*, 5590; (c) Jacobs, P. A.; Hinnekens, H., Patent EP0329923, **1989**; (d) Jae, J.; Tompsett, G. A.; Foster, A. J.; Hammond, K. D.; Auerbach, S. M.; Lobo, R. F.; Huber, G. W., *J. Catal.*, **2011**, *279*, 257; (e) Liang, G.; Cheng, H.; Li, W.; He, L.; Yu, Y.; Zhao, F., *Green Chem.*, **2012**, *14*, 2146; (f) Philippaerts, A.; Breesch, A.; Cremer, G.; Kayaert, P.; Hofkens, J.; Mooter, G.; Jacobs, P.; Sels, B., *J. Am. Oil Chem. Soc*, **2011**, *88*, 2023; (g) Philippaerts, A.; Goossens, S.; Jacobs, P. A.; Sels, B. F., *ChemSusChem*, **2011**, *4*, 684; (h) Philippaerts, A.; Goossens, S.; Vermandel, W.; Tromp, M.; Turner, S.; Geboers, J.; Van Tendeloo, G.; Jacobs, P. A.; Sels, B. F., *ChemSusChem*, **2011**, *4*, 757; (i) Philippaerts, A.; Paulussen, S.; Breesch, A.; Turner, S.; Lebedev, O. I.; Van Tendeloo, G.; Sels, B.; Jacobs, P., *Angew. Chem. Int. Ed.*, **2011**, *50*, 3947; (j) Philippaerts, A.; Paulussen, S.; Turner, S.; Lebedev, O. I.; Van Tendeloo, G.; Poelman, H.; Bulut, M.; De Clippel, F.; Smeets, P.; Sels, B.; Jacobs, P., *J. Catal.*, **2010**, *270*, 172; (k) Zapata, P. A.; Faria, J.; Ruiz, M. P.; Jentoft, R. E.; Resasco, D. E., *J. Am. Chem. Soc.*, **2012**, *134*, 8570.

(3) (a) Martens, J.; De Vos, D.; Kirschhock, C. A.; Pescarmona, P.; Sels, B.; Vankelecom, I. J., *Top. Catal.*, **2009**, *52*, 1119; (b) Sartipi, S.; Makkee, M.; Kapteijn, F.; Gascon, J., *Catalysis Science & Technology*, **2014**, *4*, 893.

(4) (a) Bejblova, M.; Cejka, J., *Synthesis of fine chemicals over zeolites*, in *Zeolites*, eds. J. Cejka, J. Perez-Pariente and W. J. Roth, Wiley Interscience, **2008**, pp. 263-297; (b) Liu, X.; Lu, M.; Ai, N.; Yu, F.; Ji, J., *Industrial Crops and Products*, **2012**, *38*, 81.

(5) (a) Beyerlein, R. A.; Choi-Feng, C.; Hall, J. B.; Huggins, B. J.; Ray, G. J., *Top. Catal.*, **1997**, *4*, 27; (b) Biswas, J.; Maxwell, I. E., *Appl. Catal.*, **1990**, *63*, 197; (c) Kung, H. H.; Williams, B. A.; Babitz, S. M.; Miller, J. T.; Haag, W. O.; Snurr, R. Q., *Top. Catal.*, **2000**, *10*, 59; (d) van Bokhoven, J. A.; Roest, A. L.; Koningsberger, D. C.; Miller, J. T.; Nachtegaal, G. H.; Kentgens, A. P. M., *J. Phys. Chem. B*, **2000**, *104*, 6743.

(6) (a) Kawai, T.; Tsutsumi, K., *J. Colloid Interface Sci.*, **1999**, *212*, 310; (b) Zukal, A.; Patzelová, V.; Lohse, U., *Zeolites*, **1986**, *6*, 133.

(7) (a) Gounder, R., *Catalysis Science & Technology*, **2014**, *4*, 2877; (b) Jacobs, P. A.; Dusselier, M.; Sels, B. F., *Angew. Chem. Int. Ed.*, **2014**, 53, 8621; (c) Okuhara, T., *Chem. Rev.*, **2002**, *102*, 3641.

(8) (a) Dimitrijevic, R.; Lutz, W.; Ritzmann, A., *J. Phys. Chem. Solids*, **2006**, *67*, 1741; (b) Ehrhardt, K.; Suckow, M.; Lutz, W., *Stud. Surf. Sci. Catal.*, **1995**, *94*, 179; (c) Lutz, W.; Gessner, W.; Bertram, R.; Pitsch, I.; Fricke, R., *Microporous Mater.*, **1997**, *12*, 131; (d) Lutz, W.; Toufar, H.; Kurzhals, R.; Suckow, M., *Adsorption*, **2005**, *11*, 405; (e) Ravenelle, R. M.; Schüßler, F.; D'Amico, A.; Danilina, N.; van Bokhoven, J. A.; Lercher, J. A.; Jones, C. W.; Sievers, C., *J. Phys. Chem. C*, **2010**, *114*, 19582; (f) Sano, T.; Nakajima, Y.; Wang, Z. B.; Kawakami, Y.; Soga, K.; Iwasaki, A., *Microporous Mater.*, **1997**, *12*, 71; (g) Zapata, P. A.; Huang, Y.; Gonzalez-Borja, M. A.; Resasco, D. E., *J. Catal.*, **2013**, *308*, 82.

(9) Tsutsumi, K.; Nishimiya, K., *Thermochim. Acta*, **1989**, *143*, 299.

(10) Geboers, J.; Van de Vyver, S.; Carpentier, K.; de Blochouse, K.; Jacobs, P.; Sels, B., *Chem. Commun.*, **2010**, *46*, 3577.

(11) Remy, M. J.; Stanica, D.; Poncelet, G.; Feijen, E. J. P.; Grobet, P. J.; Martens, J. A.; Jacobs, P. A., *J. Phys. Chem.*, **1996**, *100*, 12440.

(12) Gordon, R.; Bender, R.; Herman, G. T., *J. Theor. Biol.*, **1970**, *29*, 471.

(13) Massiot, D.; Fayon, F.; Capron, M.; King, I.; Le Calvé, S.; Alonso, B.; Durand, J.-O.; Bujoli, B.; Gan, Z.; Hoatson, G., *Magn. Reson. Chem.*, **2002**, *40*, 70.

(14) Marshall, W. L.; Franck, E. U., *J. Phys. Chem. Ref. Data*, **1981**, *10*, 295.

(15) Lutz, W., *Cryst. Res. Technol.*, **1990**, *25*, 921.

(16) (a) Triantafillidis, C. S.; Vlessidis, A. G.; Evmiridis, N. P., *Ind. Eng. Chem. Res.*, **1999**, *39*, 307; (b) Triantafillidis, C. S.; Vlessidis, A. G.; Nalbandian, L.; Evmiridis, N. P., *Microporous Mesoporous Mater.*, **2001**, *47*, 369; (c) van Donk, S.; Janssen, A. H.; Bitter, J. H.; de Jong, K. P., *Catal. Rev.*, **2003**, *45*, 297.

(17) (a) Ali, M. A.; Tatsumi, T.; Masuda, T., *Appl. Catal., A*, **2002**, *233*, 77; (b) Williams, M. F.; Fonfé, B.; Sievers, C.; Abraham, A.; van Bokhoven, J. A.; Jentys, A.; van Veen, J. A. R.; Lercher, J. A., *J. Catal.*, **2007**, *251*, 485.

(18) Lutz, W.; Löffler, E.; Zibrowius, B., *Hydrothermal and alkaline stability of high-silica y zeolites generated by combining substitution and steaming*, in *Stud. Surf. Sci. Catal.*, eds. B. Laurent and K. Serge, Elsevier, **1995**, pp. 327-334.

(19) Janssen, A. H.; Koster, A. J.; de Jong, K. P., *Angew. Chem. Int. Ed.*, **2001**, *40*, 1102.

(20) Midgley, P. A.; Weyland, M., *Ultramicroscopy*, **2003**, *96*, 413.

(21) (a) Koster, A. J.; Ziese, U.; Verkleij, A. J.; Janssen, A. H.; de Jong, K. P., *The Journal of Physical Chemistry B*, **2000**, *104*, 9368; (b) Midgley, P. A.; Dunin-Borkowski, R. E., *Nat Mater*, **2009**, *8*, 271; (c) Zečević, J.; de Jong, K. P.; de Jongh, P. E., *Curr. Opin. Solid State Mater. Sci.*, **2013**, *17*, 115.

(22) Kortunov, P.; Vasenkov, S.; Kärger, J.; Valiullin, R.; Gottschalk, P.; Fé Elía, M.; Perez, M.; Stöcker, M.; Drescher, B.; McElhiney, G.;

Berger, C.; Gläser, R.; Weitkamp, J., *J. Am. Chem. Soc.*, **2005**, *127*, 13055.
(23) (a) Fyfe, C. A.; Gobbi, G. C.; Hartman, J. S.; Klinowski, J.; Thomas, J. M., *J. Phys. Chem.*, **1982**, *86*, 1247; (b) Klinowski, J., *Prog. Nucl. Magn. Reson. Spectrosc.*, **1984**, *16*, 237; (c) Müller, D.; Gessner, W.; Behrens, H. J.; Scheler, G., *Chem. Phys. Lett.*, **1981**, *79*, 59.
(24) Klinowski, J.; Thomas, J. M.; Fyfe, C. A.; Gobbi, G. C., *Nature*, **1982**, *296*, 533.
(25) (a) Gilson, J.-P.; Edwards, G. C.; Peters, A. W.; Rajagopalan, K.; Wormsbecher, R. F.; Roberie, T. G.; Shatlock, M. P., *J. Chem. Soc., Chem. Commun.*, **1987**, 91; (b) Sanz, J.; Fornes, V.; Corma, A., *J. Chem. Soc. Faraday Trans. 1*, **1988**, *84*, 3113.
(26) (a) Bosáček, V.; Freude, D., *Stud. Surf. Sci. Catal.*, **1988**, *37*, 231; (b) Samoson, A.; Lippmaa, E.; Engelhardt, G.; Lohse, U.; Jerschkewitz, H. G., *Chem. Phys. Lett.*, **1987**, *134*, 589.
(27) Almutairi, S. M. T.; Mezari, B.; Filonenko, G. A.; Magusin, P. C. M. M.; Rigutto, M. S.; Pidko, E. A.; Hensen, E. J. M., *ChemCatChem*, **2013**, *5*, 452.
(28) Lutz, W.; Heidemann, D.; Kurzhals, R.; Kryukova, G., *Z. Anorg. Allg. Chem.*, **2010**, *636*, 1361.
(29) Cairon, O., *ChemPhysChem*, **2013**, *14*, 244.
(30) Ward, J. W., *J. Catal.*, **1970**, *18*, 348.
(31) (a) Iler, R. K.; *The chemistry of silica: solubility, polymerization, colloid and surface properties, and biochemistry*, John Wiley & Sons, USA, **1978**; (b) Kim, J. M.; Ryoo, R., *Bull. Korean Chem. Soc.*, **1996**, *17*, 66.
(32) McDonald, R. S., *The Journal of Physical Chemistry*, **1958**, *62*, 1168.
(33) Jacobs, P.; Uytterhoeven, J. B., *J. Catal.*, **1971**, *22*, 193.
(34) (a) Cho, S. J.; Jung, S. M.; Shul, Y. G.; Ryoo, R., *J. Phys. Chem.*, **1992**, *96*, 9922; (b) Verdonck, J. J.; Jacobs, P. A.; Genet, M.; Poncelet, G., *J. Chem. Soc., Faraday Trans. 1*, **1980**, *76*, 403.
(35) Thomas, J. M., *J. Mol. Catal.*, **1984**, *27*, 59.
(36) Lutz, W.; Bertram, R.; Heidemann, D.; Kurzhals, R.; Rüscher, C.; Kryukova, G., *Z. Anorg. Allg. Chem.*, **2011**, *637*, 75.
(37) Lynch, J.; Raatz, F.; Dufresne, P., *Zeolites*, **1987**, *7*, 333.
(38) Nesterenko, N. S.; Thibault-Starzyk, F.; Montouilliout, V.; Yushchenko, V. V.; Fernandez, C.; Gilson, J. P.; Fajula, F.; Ivanova, I. I., *Kinet. Catal.*, **2006**, *47*, 40.
(39) Krauskopf, K. B., *Geochim. Cosmochim. Acta*, **1956**, *10*, 1.
(40) Weast, R. C.; *CRC Handbook of Chemistry and Physics*, The Chemical Rubber Company Press, Cleveland, USA, **1972**.
(41) Batten, G. L.; *The Sizing of Paper*, TAPPI Press, Atlanta, USA, **2005**.
(42) Verboekend, D.; Vilé, G.; Pérez-Ramírez, J., *Cryst. Growth Des.*, **2012**, *12*, 3123.
(43) (a) Groen, J. C.; Jansen, J. C.; Moulijn, J. A.; Pérez-Ramírez, J., *J. Phys. Chem. B*, **2004**, *108*, 13062; (b) Groen, J. C.; Peffer, L. A. A.; Moulijn, J. A.; Pérez-Ramírez, J., *Chem. Eur. J.*, **2005**, *11*, 4983; (c) Ogura, M.; Shinomiya, S.-y.; Tateno, J.; Nara, Y.; Kikuchi, E.; Matsukata, M., *Chem. Lett.*, **2000**, *29*, 882.
(44) Verboekend, D.; Perez-Ramirez, J., *Catal. Sci. Technol.*, **2011**, *1*, 879.
(45) Verboekend, D.; Vilé, G.; Pérez-Ramírez, J., *Adv. Funct. Mater.*, **2012**, *22*, 916.
(46) Mokaya, R., *J. Phys. Chem. B*, **2000**, *104*, 8279.

TOC Artwork